Microstructure Characterization of Battery Materials Based on Voxelated Image Data: Computation of Active Surface Area and Tortuosity

To cite this article: S. Daubner and B. Nestler 2024 *J. Electrochem. Soc.* **171** 120514
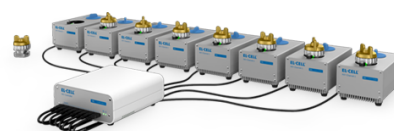
View the article online for updates and enhancements.

You may also like

Microstructure Characterization of Battery Materials Based on Voxelated Image Data: Computation of Active Surface Area and Tortuosity

S. Daubner[1,2,z] and B. Nestler[1,3]

[1]*Institute of Nanotechnology (INT), Karlsruhe Institute of Technology, 76344 Eggenstein-Leopoldshafen, Germany*
[2]*Dyson School of Design Engineering, Imperial College London, London, United Kingdom*
[3]*Institute for Applied Materials (IAM-MMS), Karlsruhe Institute of Technology, 76131 Karlsruhe, Germany*

The reliable computation of microstructure metrics such as specific surface area and tortuosity factors is key to bridge the gap between the battery microscale and fast, homogenized cell models. In this work, we present an approach to compute the surface area of phases based on pixelated image data which is both easy-to-implement and computationally efficient. The concept is inspired from the diffuse surface representation in phase-field methods. Subsequently, the approach is validated and compared with common python libraries on two benchmark cases and actual battery microstructure data. The results underline the reliability and fast computational performance of the approach. Furthermore, the concept of through-feature connectivity in pixelated image data is introduced and explored to quantify the reliability of tortuosity factor computations. Overall, this work enhances the computational tools to bridge the scale from battery microstructures to cell models and gives an overview of state-of-the-art methodology. The developed code is published to further accelerate the scientific progress in this field.

Battery performance is strongly related to the hierarchical, porous microstructure on the electrode level. The complex network of active material, pores, conductive carbon and binder is key to enable fast ionic and electronic transport within the electrode layer and, furthermore, to create short diffusion paths for the intercalated ions. Transport in the active material is strongly influenced by the structural appearance of crystalline materials on the mesoscale (i.e. single crystals with more than 100 nm and secondary particles up to 15 μm). Layered-oxides based on nickel, manganese and cobald (NMC) are state-of-the-art cathode materials and form hierarchical structures of many primary crystals agglomerated in a spherical secondary particle.[1,2] From a material design point of view, it is desirable to identify the limiting kinetic factors such that the electrode microstructure can be optimized in terms of performance for a given material. Physical modelling holds promise to guide material and microstructure design but is faced with the challenge that batteries in general and particularly hierarchical electrode structures are a multi-scale problem as sketched in Fig. 1.

Homogenized battery models like the Doyle-Newman-Fuller (DFN) cell model rely on a reduced decription of the actual electrode and particle microstructure in terms of effective properties. Spherical agglomerates which consist of many primary crystals are typically represented by the simplification of a perfectly homogenous sphere. Therefore, the diffusivity used in cell models corresponds to the apparent diffusivity (similar to PITT measurements) which is an averaged value over the respective microstructure.[3] This is particularly relevant for polycrystalline microstructures exhibiting strong texture i.e. alignment of primary crystals[4] or nano-pores which can be infiltrated by liquid electrolyte.[5] The electrode microstructure is typically reduced to a 1D transport model assuming infinite extension in the layer directions where effective properties are based on mixture theory.[6] As the Voigt-Taylor homogenization based on volume fractions typically overestimates the transport within a complex, tortuous microstructure, the tortuosity factor can additionally be considered.[7,8] The two scales are then coupled by the intercalation flux described by a Butler-Volmer type equation[6,9] or coupled ion-electron transfer[10] which depends on the active surface, i.e. surface area between electrolyte and the active material.

A necessary pre-requesite for the computation of microstructure metrics is a suitable 3D representation of the microstructure itself which is typically obtained from imaging techniques and subsequent segmentation of phases. The raw data is obtained as a stack of pixelated images e.g. by alternating Focused ion beam (FIB) milling combined with Scanning electron microscopy (SEM)[8,11] or X-ray computed tomography (CT).[12] Experimental datasets can become quite large e.g. when a 64×64 μm Section is imaged with a depth of 100–200 μm at a pixel resolution of 126.2 nm.[12] This results in roughly 200-400 million voxels of grayscale values or in terms of solving a simple PDE as the heat equation in 400 million degrees of freedom. Recently, the introduction of generative machine learning methods in the context of porous microstructures has led to a surge in available microstructure data due to their manifold possibilities of data augmentation.[5,13–15] The generation of artificial microstructures is based on the idea that these virtual structures share the same stochastic properties as the experimental input images. In the context of battery materials, the previously discussed metrics like active surface area and tortuosity factors can be used for the loss function in training models to produce realistic battery microstructures.

In both cases, large datasets and machine learning applications, the fast and reliable computation of surface area and effective transport is, thus, highly relevant. Therefore, the main focus of this work is the validation of fast and reliable algorithms to extract microstructure metrics from pixelated image data, specifically, the volume fractions of respective phases, surface area and effective transport coefficients given by the tortuosity factor. Various methods will be combined to study and disentangle two effects which arise from the pixelated representation of the structure. Namely, the two validation examples comprise a

• Sphere to study the effect of feature resolution (Fig. 2a). Pores and particles of active material in an electrode structure can be approximated as spheres and the question arises how strongly the computation of volume fractions and surface area is affected at low resolution;
• Face-centered cubic (FCC) unit cell to study the effect of contact resolution of neighbouring features and its influence on tortuosity factors (Fig. 2b).

The study is complemented by three realistic microstructures, namely a representative volume element of nano-porous NVP-C
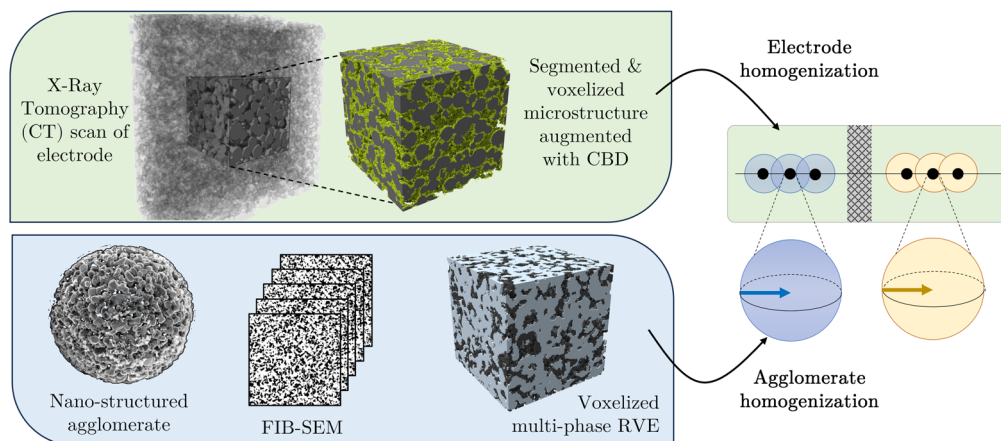
[z]E-mail: s.daubner@imperial.ac.uk

Figure 1. Integration of microstructure information from the electrode scale ($\sim$100 μm) and the active material ($\sim 1 - 10$ μm) into homogenized battery cell models. Microstructure data is taken from.[3,4]
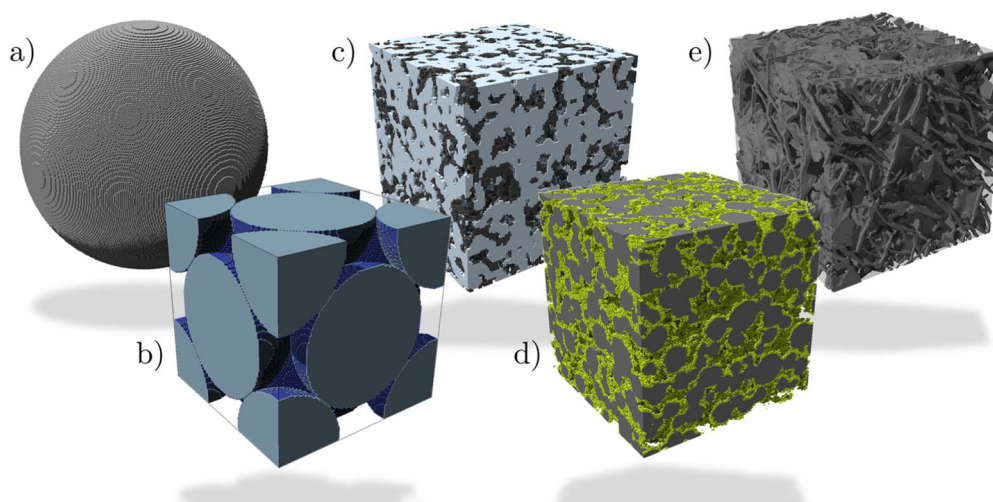

Figure 2. Overview of microstructures used in this work. Validation cases (a) voxelized sphere and (b) face-centered cubic unit cell. Application microstructures comprise (c) nano-porous sodium-ion cathode sample based on FIB-SEM[3] (d) X-ray CT of electrode, numerically augmented with carbon-binder domain (CBD)[4] and (e) graphitic flakes in ferritic matrix.[16]

which is a promising cathode material for sodium ion batteries (see Fig. 2c), a Section from a commercial NMC electrode from X-ray tomography (Fig. 2d)[4] and a biphasic iron-graphite structure (Fig. 2c) to underline the generality of the used methods. The data analysis is documented in Jupyter notebooks, which are openly available on github, including all the code necessary to reproduce the results.[17]

While this work focuses on how pixelation affects the extracted microstructural metrics, there are many other sources of uncertainty along the workflow sketched in Fig. 1 from the raw image data to the simulated cell performance. Firstly, there is the question of how representative the tomography data is, or in other words whether the volume imaged is large enough to capture the statistics of the microstructure. Secondly, there are various approaches to segmentation which deliver different outputs, and so this step introduces uncertainty that propagates into the subsequent steps.[18–20] A methodology to quantifiy this uncertainty and its propagation into microstructure metrics is presented by Krygier et al.[19] The relationship to effective transport properties can be highly nonlinear as adding pixels not only changes the resolution of microstructural features but might also connect previously disconnected areas. The susceptibity of tortuosity computation to segmentation uncertainty has been illustrated based on X-ray CT data of graphite electrodes,

along with a discussion of spatial heterogeneity.[20] Lastly, cell models rest on simplifying assumptions and the variation of input parameters is often neglected. The work by Laue et al.[21] shows how the variance of cell production parameters influences the expected cell performance. Ultimately, the validation of this digital workflow with experimental cell data[22] is key to enable meaningful microstructure optimization for battery design.[23]

Methodology

All computations of microstructure metrics are based on voxelized structures as obtained from tomography methods. The numerical implementation and testing is done using python including common libraries such as *scikit-image*, *porespy* and *tau-factor*. The source code to fully reproduce this study is made openly available.[17]

Volume fraction.—The volume fraction of a phase $\varepsilon\alpha$ if defined as its volume divided by the total volume of the domain $\varepsilon\alpha = V_\alpha/V$. If phases are represented by discrete grayscale values in a voxel grid ($B: \mathbb{R}^3 \in L \times M \times N$), the volume fraction of a phase is defined as the sum of all voxels that match the grayscale value of a phase divided by the total number of voxels in the domain

$$\varepsilon\alpha = \sum_i \sum_j \sum_k (b_{ijk} == \text{grayscale value})/(LMN). \qquad [1]$$

Specific surface area.—The specific surface area of a phase α is defined as the ratio of the surface over the domain volume $a_\alpha = A_\alpha/V$. As the phases are represented by a voxel grid, there are multiple ways to compute the surface area, e.g.

- Count faces between different phases in the voxel grid;
- Compute a new surface representation (triangulated mesh) using a marching cubes algorithm and then compute the surface area as the sum of triangle areas;
- Employ the concept of diffuse surface representation from the phase-field method where $A = \int_V |\nabla \phi| dV$ and ϕ is an indicator function.

Conceptually, counting the faces between differently labelled voxels is the simplest method and, intuitively, we expect large errors to arise from the zig-zagging of curved surfaces. The *marching cubes* algorithm introduced by Lorensen and Cline[24] in 1987 has become a standard tool which can be found in common open-source packages such as *scikit-image*.[25] The implementation includes the advancements made by Lewiner et al.[26] For the context of this work we employ a function based on *scikit-image* which first extracts the vertices of a triangulated mesh and subsequently computes the surface area. Additionally, a function implemented in *porespy* which is based on the scikit-image marching cubes in combination with smoothing is used for comparison.[27,28]

Within the phase-field approach, interfaces are described by a smooth but steep transition of an order paramter ψ (therefore often called a 'diffuse interface'). In the following we restrict the values of $\psi \in [0, 1]$ and, thus, ψ can be interpreted as the local volume fraction of a respective phase. The free energy functional consists of a gradient term and a homogenous part[29,30] (more details in Appendix A)

$$\mathcal{F} = \gamma \int_V \epsilon |\nabla\psi|^2 + \frac{9}{\epsilon}\psi^2(1-\psi)^2 dV \qquad [2]$$

where γ has units of [J/m²] and ϵ [m] scales the width of the diffuse interface. Based on Hamilton's principle and linear relaxation of the system free energy with a mobility factor M, the evolution equation is given by

$$\dot{\psi} = -2M\gamma\left(\frac{9}{\epsilon}\psi(1-2\psi)(1-\psi) - \epsilon\nabla^2\psi\right). \qquad [3]$$

Equation (3) leads to the formation of a diffuse interface and an evolution of the microstructure driven by curvature minimization. Based on the analytical considerations in Appendix A, the surface area of arbitrary complex morphologies can be described by a volume integral (Eqs. (A3)–(A7)). Variant Eq. (A6) converges much faster than the other expressions and even yields a good estimate of the surface area in the initial binary case where all voxels have values of either one or zero. Therefore, we employ

$$A_{\text{gradient}} = \int_V |\nabla\psi| dV \qquad [4]$$

for computation of the specific surface area and compare this method to other common approaches. The gradient is calculated based on a second-order finite difference stencil as described in the Algorithm 1 directly on the voxelized structure which coincides with a regular grid.

Algorithm 1. Computation of specific surface area based on gradient norm in python format based on the *numpy* package

```
def specific_surface_area(array, dx=1.0, dy=1.0, dz=1.0):
  gradx = numpy.gradient(array, axis=0)/dx
  grady = numpy.gradient(array, axis=1)/dy
  if array.ndim == 2:
    gradient_norm = numpy.sqrt(gradx**2 + grady**2)
  elif array.ndim == 3:
    gradz = numpy.gradient(array, axis=2)/dz
    gradient_norm = numpy.sqrt(gradx**2 + grady**2 + gradz**2)

  surface_area = numpy.sum(gradient_norm)
  volume = numpy.prod(array.shape)*dx*dy*dz
  return = surface_area/volume
```

Tortuosity factors.—The effective conductivity/diffusivity of a porous material is related to its bulk properties by the volume fraction and the tortuosity factor τ which accounts for geometric effects of the microstructure. Both steady-state diffusion and electrical conduction are described by the partial differential equation

$$\nabla\cdot(\Gamma\nabla u) = 0 \qquad [5]$$

where Γ can be the bulk diffusivity $D_{\alpha,0}$ or electrical conductivity $\sigma_{\alpha,0}$. Following the works of[12] and[9] the tortuosity factor τ_α can be expressed as

$$\frac{\tau_\alpha}{\varepsilon\alpha} = \frac{\Gamma_{\alpha,0}}{\Gamma_\alpha^{\text{eff}}} = \frac{D_{\alpha,0}}{D_\alpha^{\text{eff}}} = \frac{\sigma_{\alpha,0}}{\sigma_\alpha^{\text{eff}}} \qquad [6]$$

where $\varepsilon\alpha$ denotes the volume fraction as defined above. The open-source application taufactor[9,31] is employed to compute the effective properties based on a finite difference scheme.

The second-order finite difference scheme calculates fluxes across the sides of neighbouring voxels. Two voxels of the same phase which only share an edge or corner will thus be considered disconnected in the numerical scheme. This plays a major role for the computation of tortuosity factors at low resolution of features and contact areas. In this sense, the evaluation of connectivity, especially the "through-feature" connectivity, can be utilized to quantify the uncertainty arising from low resolution of a voxelized structures. The through-feature connectivity (TF-conn) is defined as the fraction of conducting material which connects both ends of the investigated flux direction as sketched in Fig. 3a. Every individual region is assigned an integer number as a label and thus the spanning labels can be found by checking which labels occur at both sides of the cube. This can be checked for all three spatial directions individually. In the sketched example in Fig. 3a the labels 2 and 4 span the whole volume from left to right side. Label 3 is considered disconnected from label 2 based on side connectivity (Fig. 3b) while both features would unite for edge and corner connectivity (Figs. 3c and 3d). If the through-feature fraction changes considerably depending on the chosen contact definition of neighbouring voxels (side, edge or corner) as shown in Figs. 3b–3d, the dataset suffers from large uncertainty due to low contact resolution. When the tortuosity factor is computed based on the extracted through-features, the relation

$$\Gamma_\alpha^{\text{eff}} = \frac{\epsilon_\alpha^{\text{TF}}}{\tau_\alpha^{\text{TF}}}\Gamma_{\alpha,0} = \frac{\epsilon_\alpha}{\tau_\alpha}\Gamma_{\alpha,0} \rightarrow \tau_\alpha = \frac{\epsilon_\alpha}{\epsilon_\alpha^{\text{TF}}}\tau_\alpha^{\text{TF}}$$
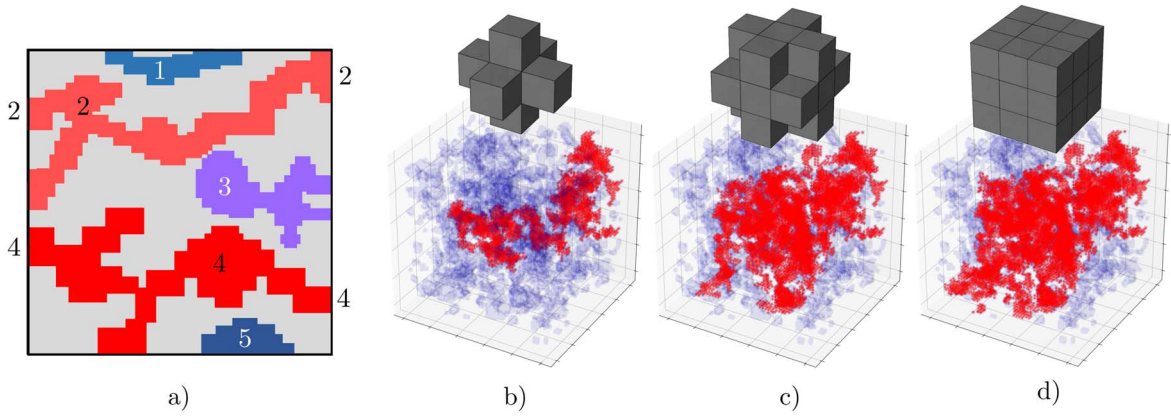
Figure 3. Visualization of the through-feature connectivity. (a) Sketch of exemplary structure where the labels 2 and 4 would be the through-features in x-direction. Evaluation of connectivity network based on (b) side, (c) edge and (d) corner connectivity for a NVP microstructure taken from[3]. Red areas are connected while blue denotes the phase fraction which is inactive for transport.
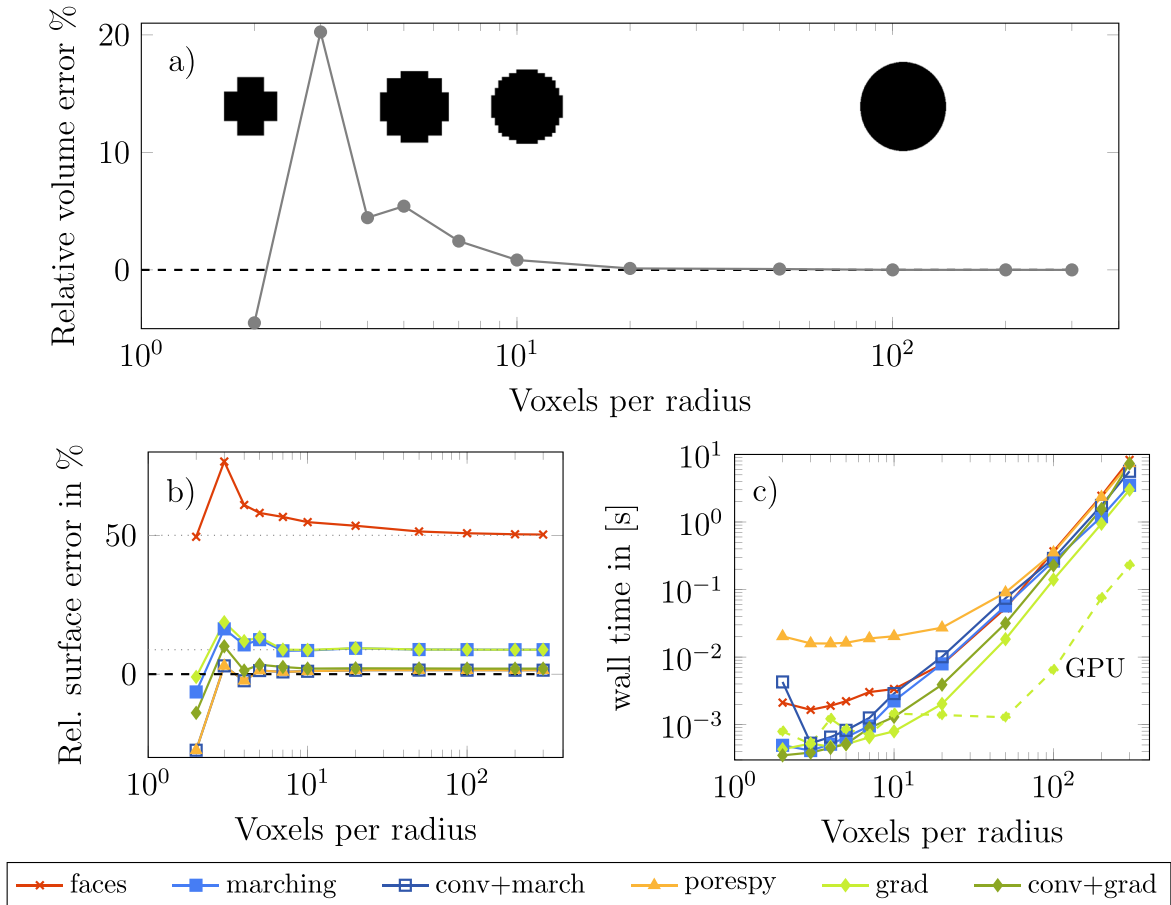

Figure 4. Comparison of microstructure metrics for various resolutions of a sphere on a voxel grid. The relative volume error is shown in (a), the relative error of surface area computation is shown for various methods in (b) together with the corresponding wall time for surface determination in (c).

holds, where ϵ_α and τ_α are the relevant quantities for standard DFN models. Note that directly working with the effective properties D_α^{eff}, $\sigma_\alpha^{\text{eff}}$ is more intuitive and less prone to errors.

Results and Discussion

Validation 1: Voxelized sphere.—The simplest three-dimensional validation example including curvature is a sphere for which the volume and surface area can be analytically expressed as a function of the radius. This validation is relevant for porous battery microstructures as many pore features and particles exhibit a nearly spherical shape. To study the influence of spatial feature resolution, we vary the amount of voxels per radius and compute the relative error of the volume and surface area with respect to the analytical solution. The results in Fig. 4a show that the volume error converges toward zero as the sphere is resolved with more voxels.

The computation of surface area by counting faces converges toward a relative error of 50% (Fig. 4b). This can be analytically explained by the fact that the projection of a sphere onto a plane (sort of the shade) equals an area of πR^2. Therefore, counting faces on a
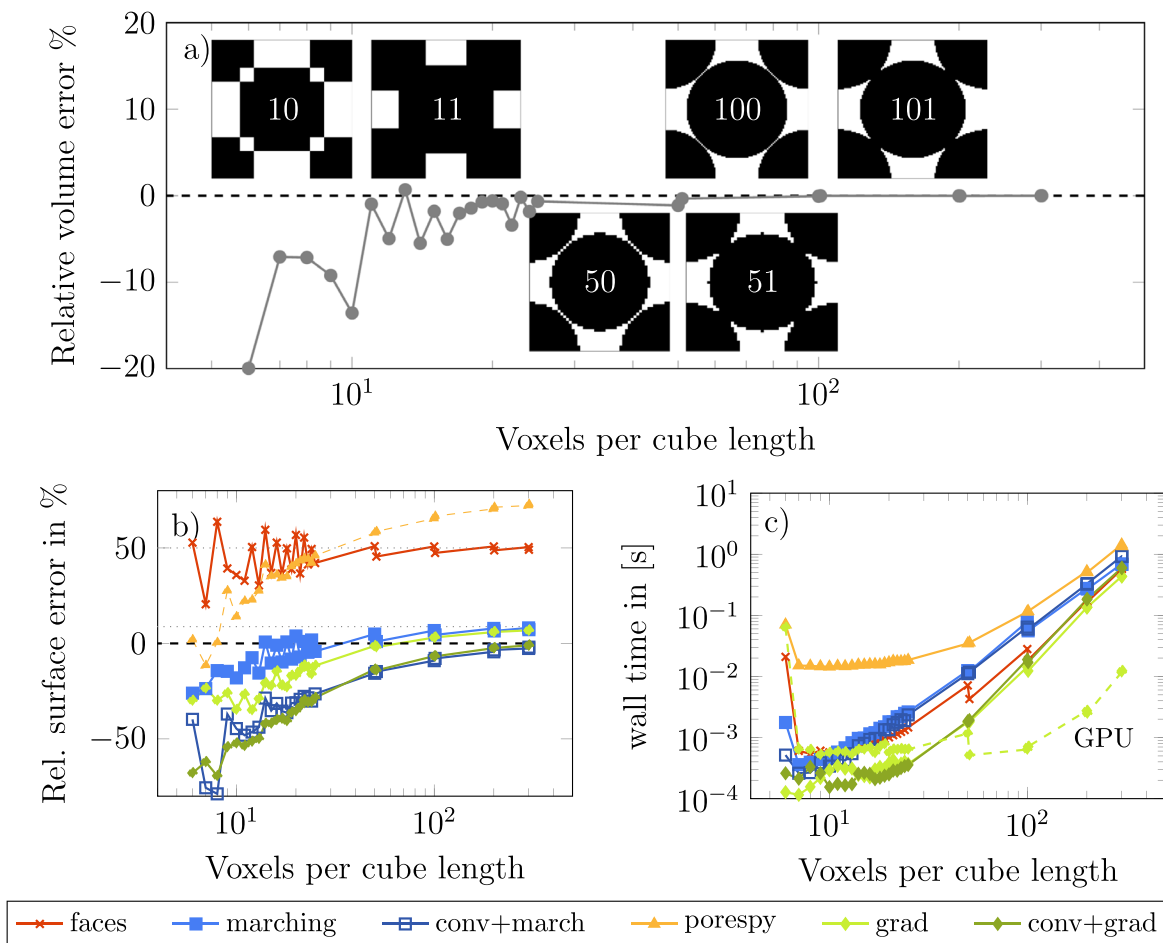
Figure 5. Validation of volume fraction and surface area computation on voxelized FCC structure. The relative volume error is shown in (a), the relative error of surface area computation is shown for various methods in (b) together with the corresponding wall time for surface determination in (c).

3D voxelized grid equals $6\pi R^2$ in the limit of high resolution. The analytical sphere surface area is given by $4\pi R^2$, i.e. the expected convergence of the relative error is 50%. The marching cubes method and the gradient based approach both converge to a relative error of 8.8% which can be significantly lowered if the initially sharp representation of the sphere is smoothened e.g. by convolution of a spherical structuring element with the initial array. After convolution, the relative error of both methods quickly converges to a relative error below 3% for more than 5 pixels per radius. In the context of the phase-field method this smoothing has a physical interpretation as it brings the initial binary field closer to the diffuse interface which would be the equilibrium solution of the phase-field evolution equation. The relative error of the gradient-based method (Eq. (4)) can be further reduced by solving the phase-field evolution equation Eq. (3) to below 1% but this comes at the computational cost of solving the PDE. The elapsed computation times for the various methods shown in Fig. 4 (c) highlight that the surface area determination based on the gradient norm (lime green line) is faster compared to all other approaches. Furthermore, the implementation of algorithm 1 utilizing *pytorch* is straightforward and leverages additional computation time savings based on GPU parallelization (solid lines refer to CPU, dashed line to GPU).

Validation 2: Face-centered cubic unit cell.—As the second validation example we investigate an FCC unit cell at various resolutions. It increases the complexity of the first validation by adding contact between spherical bodies while the volume fraction and surface area can still be expressed analytically as a function of the unit cell side length. As depicted in the inset pictures of Fig. 5a a voxelization issue arises where for all configurations with an even

number of voxels per cube length the spheres are touching at voxel edges while for all odd configurations the spheres are fully connected. The evaluation of the relative volume error shows fast convergence and low deviation for resolutions above 30^3 voxels. The relative surface error of the face counting converges to an error of 50% as discussed above.

The marching cubes and gradient-based methods yield similar results both in the case of direct evaluation on the binary image (see "marching" and "grad" in Fig. 5b) as well as after smoothing by convolution ("conv+march" and "conv+grad"). Note that the method implemented in *porespy* is also based on convolution and subsequent marching cubes but there is an additional step included where the original field is padded and, thus, the surface areas on the sides of the cube are also added to the calculation. This is not desirable for the computation of active surface area from battery electrode data and also leads to the large errors in this validation example. As in the previous example, the gradient-based method exhibits the fastest computation times as shown in Fig. 5c.

The FCC example can also be used to evaluate the computation of tortuosity factors. As the initial FCC structure has no overlap between the spherical bodies, the problem is ill-posed in the sense that the spheres are in contact at one point but there is no area e.g. for electrical conduction. In the voxelized structure, we find alternating cases of 0 and 100% through-feature connectivity as shown in the inset pictures of Fig. 5a. This means that for any even number of voxels periodic labelling based on side connectivity will result in four individual spheres while for an odd number of voxels we find one large interconnected feature. As a result, the tortuosity factor alternates between a finite value and infinity. As the resolution is increased the values diverge toward infinity as shown by the dark
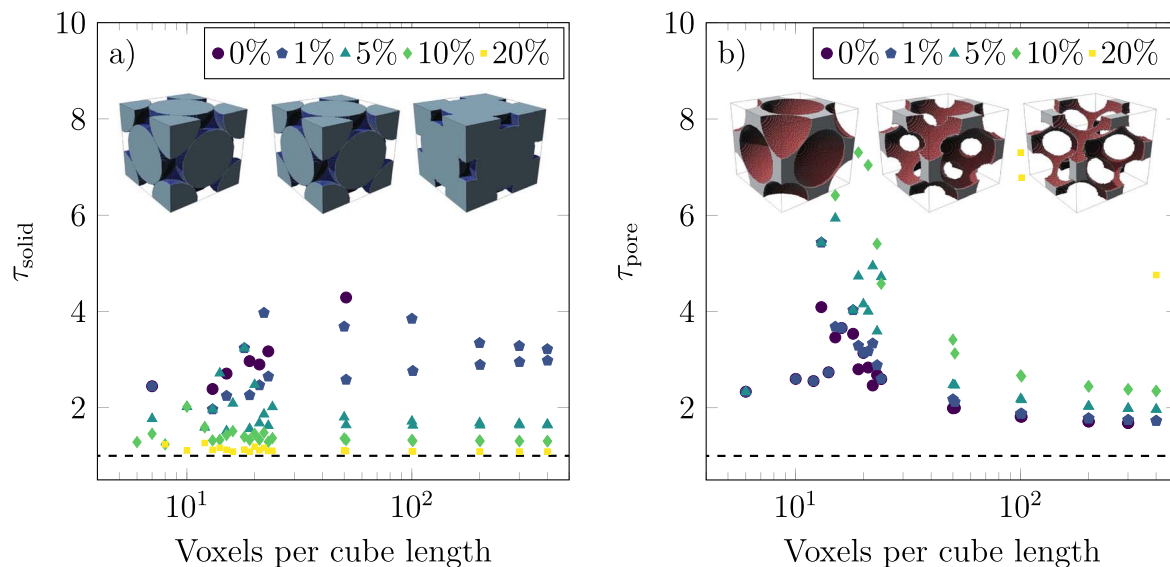
Figure 6. Tortuosity factors for various voxel resolutions and relative overlaps of 0, 1, 5, 10 and 20 percent. Results for the solid fraction are shown in (a) while the pore tortuosity factor is shown in (b).
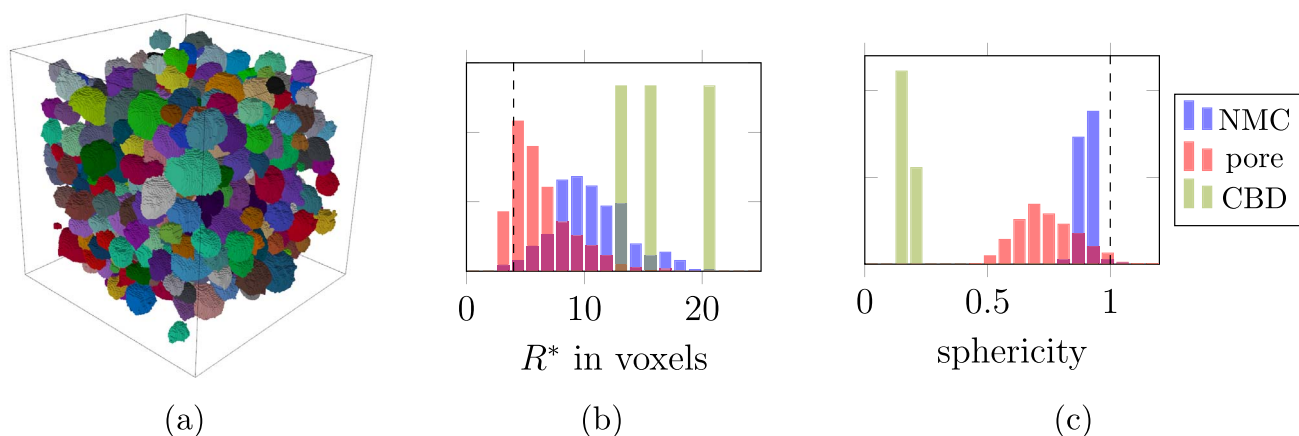

Figure 7. Feature analysis after watershed segmentation with the SNOW algorithm[33] which yields e.g. the NMC features shown in (a). For all extracted features of NMC, pore and CBD the resulting distribution of feature volumes is given in terms of the corresponding radius R^* in (b) together with the sphericity of extracted features in (c).

blue circles in Fig. 6a. To study the convergence of tortuosity factors, we introduce overlap between the spheres to ensure connectivity. In the following, the relative overlap is defined as the overlapping length divided by the sphere radius, i.e. an overlap of 100% would correpond to the case where the radius of both spheres equals the distance between their midpoints. Accordingly the volume and surface area of the resulting FCC unit cell can be computed by substracting the spherical caps defined by the overlap at the 24 contact points inside the structure.

As the overlap is increased, the tortuosity factor for the solid fraction is decreased. The case of 1% overlap features strong oszillations with values jumping in the range of $\tau_{solid} \in [2, 4]$. For an overlap of 5%, 10% and 20%, the values of τ_{solid} converge toward 1.66, 1.30 and 1.09, respectively. We observe the opposite trend for the tortuosity factor in the pore phase i.e. for increasing overlap the value τ_{pore} increases due to the reduced and more tortuous pore space (as visualized by the inset pictures in Fig. 6b). Generally, strong scatter is observed at lower resolutions while for cubes with more than 40^3 voxels the values start converging. For the surface area, the same trend as in Fig. 5b is observed for increased overlap as shown in the appendix (Fig. B1).

Electrode structure.—As an example on the electrode scale we employ raw data from the work of Usseglio-Viretta et al.[4] which has been openly provided in the repository.[32] The three-phase sample contains 50.6 vol% Nickel-Manganese-Cobald layered oxide (NMC) particles as active cathode material together with 13.4% carbon-binder domain (CBD) and 36.0% pores. The NMC particles were imaged using X-ray CT with a pixel resolution of 398 nm while the CBD has been added later based on modelling assumptions. The visualization in Fig. 2d indicates that the NMC phase consists of almost spherical particles that are relatively well resolved, while the CBD appears to be quite pixelated. To quantify this visual impression, a watershed segmentation (SNOW[33]) is performed for each phase. We then extract all features that are not in contact with the domain boundaries to avoid artefacts and calculate the corresponding feature volumes and areas. The result of the segmentation is exemplarily shown for the NMC phase in Fig. 7a.

The analysis confirms that the NMC phase consists of features with high sphericity (mean value of 0.91; a perfect sphere corresponds to 1) and an average feature radius of 10.5 voxels. Therefore, we conclude that both the volume fraction and surface area can be determined with a low error of $< 5\%$. The distribution
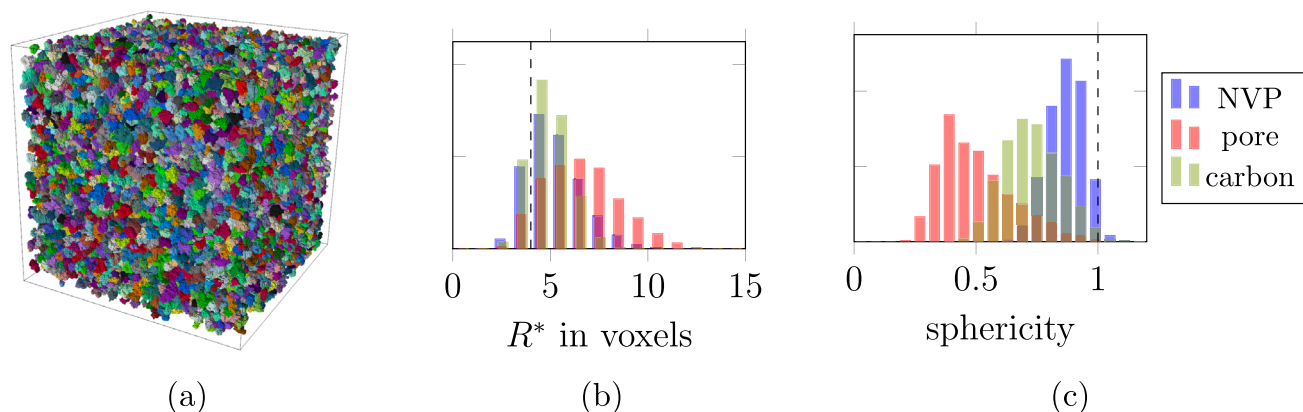
Figure 8. Distribution of (a) equivalent feature radius R^* and (b) sphericity of extracted features derived from watershed segmentation with the SNOW algorithm.[33]

Table I. Tortuosity factors of NMC, CBD and the pore fraction in all three directions.

	NMC	CBD	pore
τ_x	2.32	11.60	2.71
τ_y	2.48	12.00	2.80
τ_z	3.48	15.56	3.30

of pore volumes peaks close to the filter used in the SNOW segmentation (structuring element with radius of four pixels, corresponds to black dashed line in Fig. 7b), more details in Ref. 33) which indicates that the pore features are actually smaller and, thus, not well-resolved. For the CBD, only three features which do not touch the domain boundaries are found (green bars in Fig. 7b) and, consequently, the volume distribution is not representative. Due to the low resolution of the CBD domain it is not possible to reliably extract smaller features and analyze their distribution using the watershed segmentation. The pairwise surface area is computed based on the phase-specific surface areas[8] as

$$A_{\text{NMC–pore}} = \frac{1}{2}(A_{\text{NMC}} + A_{\text{pore}} - A_{\text{CBD}}). \quad [7]$$

Based on the results from the two benchmark cases we employ the evaluation of the gradient norm with convolution to compute specific surface areas. For the active surface area between the cathode material and the electrolyte we compute a value of 0.12 μm^{-1}. In the original publication a value of 0.1 μm^{-1} was estimated based on the crude approximation of $A_{\text{NMC}} = 3\varepsilon_{\text{NMC}}/r_p$ where r_p denotes the mean radius of active material particles. It should be noted that this value has a large uncertainty due to the low resolution of the pore space and CBD.
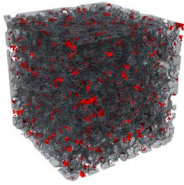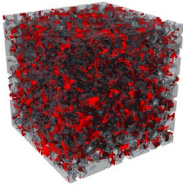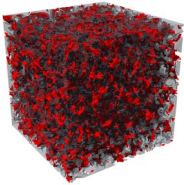
All phases are highly connected with 99.7% (NMC), 97.7% (CBD) and 99% (pore) based on side connectivity and homogeneously distributed such that identical values are obtained along the three spatial dimensions. The tortuosity factors exhibit an anisotropy in the z-direction which coincides with the direction normal to the current collector. Within the pore space we compute values of τ_{pore} = 2.7 and 2.8 in the x- and y-direction while in the z-direction τ_{pore} = 3.3. The same anisotropy is observed for the other phases as shown in Table I. The results are consistent with the reported values and anisotropy in Ref. 12.

Nanoporous NVP-C.—Sodium vanadium phosphate Na$_3$V$_2$(PO$_4$)$_3$ (NVP) is a promising cathode material for sodium ion batteries. Due to the intrinsically low electronic conductivity of NASICON crystal structures, this material can only be used at technically relevant (dis-)charging rates if it is produced as a composite of NVP and carbon (NVP/C).[34] Particle agglomerates can be produced as nano-porous spherical particles to enhance the rate capability and cycle life resulting in a quite complex three-phase microstructure.[3] The general goal is to optimize such a composite for a high fraction of active matrial (NVP), reduce the carbon content to the minimum where it is still fully connected to ensure fast electronic transport and, thirdly, ensure full connectivity of the pore network to allow for fast ionic transport in the electrolyte. The surface area between active material and the electrolyte should be maximized to allow for fast intercalation.

Therefore, we apply the aforementioned methods on the voxelized data provided along with the work of Neumann et al.[3] which has been generated by stochastic modelling based on FIB-SEM tomography data as well as high-resolution SEM images. The content of NVP is fixed to 60 vol% while the fraction of carbon and, thus, the pore space is varied. Feature analysis based on watershed segmentation is performed as described in the previous section. The distribution of equivalent feature radii R^* in Fig. 8(b) reveals that all phases exhibit a skewed distribution with its peak close to the resolution threshold, indicating low feature resolution and large uncertainty. The microstructure is highly representative in the sense that there are many features of each phase within the given domain ($\approx$20 000 for NVP as shown in Fig. 8(a), but the resolution is not sufficient for reliable extraction of microstructure metrics. For this particular example, an RVE with half the cube length but double the resolution would probably be appropriate for further analysis.

An overview of the microstructure metrics obtained for three different carbon contents is given in Table II. These examples mark the extreme cases of the data given in Ref. 5 Fig. 6d–6e. As soon as a

Table II. Nanostructured NVP/C composites with 60 vol% NVP and varying volume fractions of carbon and pore.

Carbon network

ε_{carbon}	15%	27.5%	30%
ε_{pore}	25%	12.5%	10%
$A_{NV\,P-pore}$ [1/μm][a]	7.74 (8.68)	4.14 (4.18)	3.38 (3.31)
TF-conn carbon[b]	0.82% (0.96/0.97)	0.99% (1.0/1.0)	0.99% (1.0/1.0)
TF-conn pores	0.98% (0.99/0.99)	0.44% (0.83/0.88)	0.0% (0.31/0.56)
τ_{carbon}	69.6 (69.5)	5.8 (5.8)	4.8 (4.8)
τ_{pore}	7.9 (7.9)	909.0 (1007.5)	∞ (∞)

[a] Values are computed based on convolution plus gradient. Values in brackets are based on evaluation of the gradient norm directly on the binary data. [b] The through-feature connectivity (TF-conn) reported here corresponds to the fraction of the respective phase which is fully connected in the x-direction of the cube. The structures are highly isotropic i.e. calculated values in the y- and z-direction were identical. The first value corresponds to the side connectivity which coresponds to the finite difference stencil used for computation of the tortuosity factor. The values given in brackets correspond to the edge and corner connectivity, respectively.

phase reaches a low volume fraction of 15% or below (carbon in the first case, pore in the other two cases) its respective through-feature connectivity starts to decrease. Isolated islands are formed but the variation in TF-conn values indicates that this might be an issue of low contact resolution in the voxelized data. In the first example of $\varepsilon_{carbon} = 0.15$, 82% of the carbon is connected in terms of side sharing voxels while 96% are connected if edge sharing is taken into account. Therefore, we expect the tortuosity factor of τ_{carbon} to be an overestimation due to low contact resolution. Likewise, the connectivity of the pore phase drops as the carbon fraction is increased.

While *taufactor* converges fast in most cases, it seems like values at low connectivity and thus high tortuosity factors are causing problems. When inserting the voxeldata as initally given, the tool converged in 901 iteration to $\tau_{pore} = 7.9$ while values of 85.2 and 127.5 at higher carbon fractions are both returned as converged after 101 iterations. This seems questionable from a numerical point of view as the PDE solution in a highly tortuous structure differs more strongly from the homogenous initial condition and, thus, should take more iterations to converge. For $\varepsilon_{carbon} = 30\%$ the side connectivity of pores is zero which means that there is no fully connected pathway for ionic conduction and the corresponding tortuosity factor should be infinity but the value of 127.5 is returned. Alternatively, we can extract the through-feature based on side connectivity first which is then inserted into the tortuosity calculation. Based on this two-step procedure the values in Table II were obtained. We also tried to employ the tortuosity calculation which is available in *porespy* and based on the same definition given in Eq. (6) but none of the simulations converged. The tortuosity factors given in brackets in Table II were obtained with a code from the work of Hoffrogge et al.[35] which also shares the same definition given in Eq. (6). The implementation is based on a second-order finite difference stencil but in contrast to *taufactor* a multi-grid approach is used for convergence. Additionally, the through-feature connectivity is computed beforehand such that the PDE is only solved in the connected fraction of the respective phase. The τ values given in Table II correspond to the x-direction as the structures are isotropic i.e. little directional dependence is observed.

Based on out findings, we recommend to extract the connected fraction of a phase based on side connectivity before computing tortuosity factors. If there is a considerable jump in the TF-conn values (side, edge, corner), this is a clear indication of poor resolution of the contact surfaces. We observe a very close match between the resulting tortuosity factors obtained from the two different implementations for $\tau < 100$ and some deviation at higher values of τ. This can be rationalized by the fact that the convergence

of simulations on highly tortuous structures becomes very sensitive to the chosen convergence criteria which differ between the two implementations.

Ferrite with graphitic flakes.—The methodology discussed within this work is agnostic to the actual application and can be equally applied to other voxelized microstructure data. This is exemplarily shown for an iron microstructure which is composed of a ferrite matrix and a network of graphite flakes. The data is taken from *microlib*[16] and is based on image data obtained by Dr. Cochrane at the Department of Materials, University of Leeds. The structure is shown in Fig. 2e. The ferrite matrix has a volume fraction of 77.5% and based on the voxel size of 1.375 μm the specific surface area between the two phases equals 0.13 μm^{-1}. Both phases exhibit a high connectivity of 100% (ferrite) and 99% (graphite) in all three spatial directions. For this type of material, the calculation of tortuosity factors could be relevant in the context of effective heat conduction or electrical conduction. The respective tortuosity values are $\tau_{ferrite} = 1.98$ and $\tau_{graphite} = 3.36$. If kinetics are determined by a mixed conduction, the multi-phase solver of *taufactor* could be employed.[31]

Conclusions

The reliable computation of microstructure metrics from available image data is a key aspect to transfer the complex microstructure information into coarse-grained cell simulation models based on porous electrode theory. In this context we investigate the computation of active surface area and tortuosity factors.

Firstly, we propose an approach for surface area computation based on the phase-field method which is both easy to implement and computationally efficient. Based on the two benchmark cases presented in this work, we prove that the method yields a good estimation of surface area with an error below 5% at high enough voxel resolution. The accuracy is comparable to the marching cubes algorithm while we achieve faster computation times for all benchmark simulations. Subsequently, the method is succesfully applied to battery tomography data of a sodium-ion cathode material and an NMC electrode Section obtained from X-ray CT. The computation is robust and obtained results are in good agreement with previously published results on the same image data. The implementation based on *pytorch* which leverages GPU parallelization achieves 10 times faster computation of the specific surface area across all benchmark cases and microstructure examples. The code is made openly available on github.[17]
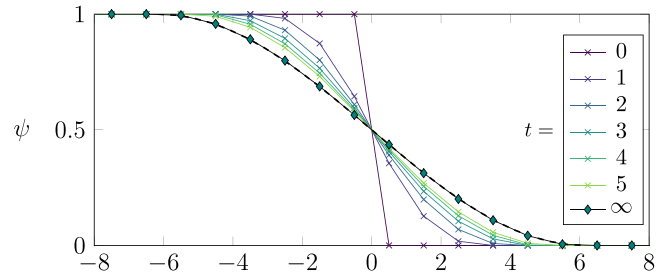
Figure A1. Evolution of a one-dimensional diffuse interface toward the equilibrium solution for $\Delta x = 1$ and $\epsilon = 5$.

$\psi^2(1-\psi)^2$) the coexistence of two phases can be naturally described with a diffuse transition between the two states. More detailed information about the phase-field method can be found in the literature.[37–39]

Starting from a pixelated and segmented image with values of 0 and 1, the computation of the evolution equation (3) leads to a smoothing of the initially sharp jump as shown in Fig. A1.

The one-dimensional steady state solution of Eq. (3) is given by $\dot{\psi} = 0$ which yields

$$
\begin{aligned}
\epsilon \nabla^2 \phi &= \frac{9}{\epsilon} \psi (1 - 2\psi)(1 - \psi) \rightarrow \epsilon \left(\frac{\partial \psi}{\partial x}\right)^2 \\
&= \frac{9}{\epsilon} \psi^2 (1 - \psi)^2 \rightarrow \mathrm{d}x = \frac{\epsilon}{3\psi(1-\psi)} \mathrm{d}\psi
\end{aligned}
\qquad [\text{A1}]
$$

The prefactors of the two energy terms in the energy functional Eq. (2) are chosen such that the surface energy of a flat interface σ equals the parameter γ as it is defined as the excess Gibbs free energy across the diffuse region

$$
\begin{aligned}
\gamma &= \gamma_{\text{ref}} \int_{-\infty}^{\infty} \epsilon |\nabla \psi|^2 + \frac{9}{\epsilon} \psi^2 (1 - \psi)^2 \mathrm{d}x \\
&= 2\gamma_{\text{ref}} \int_0^1 3\psi (1 - \psi) \mathrm{d}\psi = \gamma_{\text{ref}}.
\end{aligned}
$$

The double-well potential in combination with the gradient term, results in the equilibrium profile $\psi = 0.5 + 0.5 \tanh(3x/2\epsilon)$ and the interfacial width can be defined by the linear tangent fit in $\psi = 0.5$ such that

$$
l_{\text{int}} = \frac{1}{\mathrm{d}\psi/\mathrm{d}x}\Big|_{\psi=0.5} = \frac{4\epsilon}{3}.
\qquad [\text{A2}]
$$

If Eq. (3) is only used to parametrize an arbitrary geometry, there is no physical mobility M or interfacial energy γ involved in the problem setup which is why we set both values to 1. ϵ can be defined depending on the grid spacing Δx, e.g. as $\epsilon = 3\Delta x$ which results in a steep transition of ψ from 0 to 1 across approx. 4 cells, while most of the other values are close to 0 or 1. The volume of any shape which is parametrized by ψ is given by $V_\psi = \int \psi \mathrm{d}V$. The surface is implicitly described by the volumetric region where ψ transitions from zero to one and, hence, the surface area can also be expressed in terms of a volume integral. From the equalities in Eq. (A1) we can derive five possible measures of the surface area

$$
A_1 = \int_V \epsilon |\nabla \psi|^2 + \frac{9}{\epsilon} \psi^2 (1 - \psi)^2 \mathrm{d}V,
\qquad [\text{A3}]
$$

$$
A_2 = 2 \int_V \epsilon |\nabla \psi|^2 \mathrm{d}V,
\qquad [\text{A4}]
$$

$$
A_3 = 2 \int_V \frac{9}{\epsilon} \psi^2 (1 - \psi)^2 \mathrm{d}V,
\qquad [\text{A5}]
$$

Secondly, the concept of through-feature connectivity is introduced and applied to all microstructure examples to quantify the validity of tortuosity factor calculations. The results on NVP/C microstructures in Section Nanoporous NVP-C show that a lower TF-conn value (less connectivity) leads to an increase in tortuosity values. We find that in such cases, τ values computed on the whole phase differ strongly from computation on the connected fraction. Therefore, the recommendation is to follow a two-step procedure of extracting the connected through-feature as described in Section Methodology before computing tortuosity values. At the same time the available tools to compute τ face numerical problems with convergence at low connectivity which makes the computed values questionable from two aspects. The discrepancy between side connectivity and edge connectivity hints toward bad contact resolution on the given voxel grid and, therefore, adds uncertainty to the computation of taufactors. This effect can be mitigated if the pixel resolution is refined either directly during the imaging process or with super-resolution techniques during postprocessing.

Overall, this article describes various methods and their reliability for the calculation of effective properties of battery structures on the basis of tomography data. While the proposed methods reduce the computational cost of surface area determination and the robustness of tortuosity calculations, the application examples in Sects. Electrode structure and Nanoporous NVP-C also highlight a severe limitation: The feature resolution of available battery microstructures is not sufficient to extract microstructure metrics within defined uncertainty limits. Improved imaging techniques and data fusion methods[36] hold promise to solve this issue. In the context of ever improving imaging techniques and the rich possibilities of data augmentation by using machine learning, the importance of robust and computationally fast methods for microstructure characterization is fundamental to accelerate the development of new battery concepts.

Author Contributions

S. Daubner: conceptualization, methodology, software and simulations, writing - original draft, visualization. B. Nestler: writing - original draft, project administration and funding acquisition. All authors read and approved the final manuscript.

Data Availability

All methods developed for this study are written in the Python programming language. The studies are documented as jupyter notebooks and made available as open source software on github.[17]

Appendix A. Phase-field Method

Phase-field models rest on the idea that the free energy of a small volume of non-uniform solution can be expressed as the sum of two contributions, one being the homogenous part and one is the so-called gradient term.[29] The gradient term $|\nabla \psi|^2$ is a non-local energy induced by the gradient of e.g. concentration or phase state. In combination with a homogenous energy which features two or more energetic minima (a regular solution was used in the works of Cahn and Hilliard;[29] here we use a simple double well potential
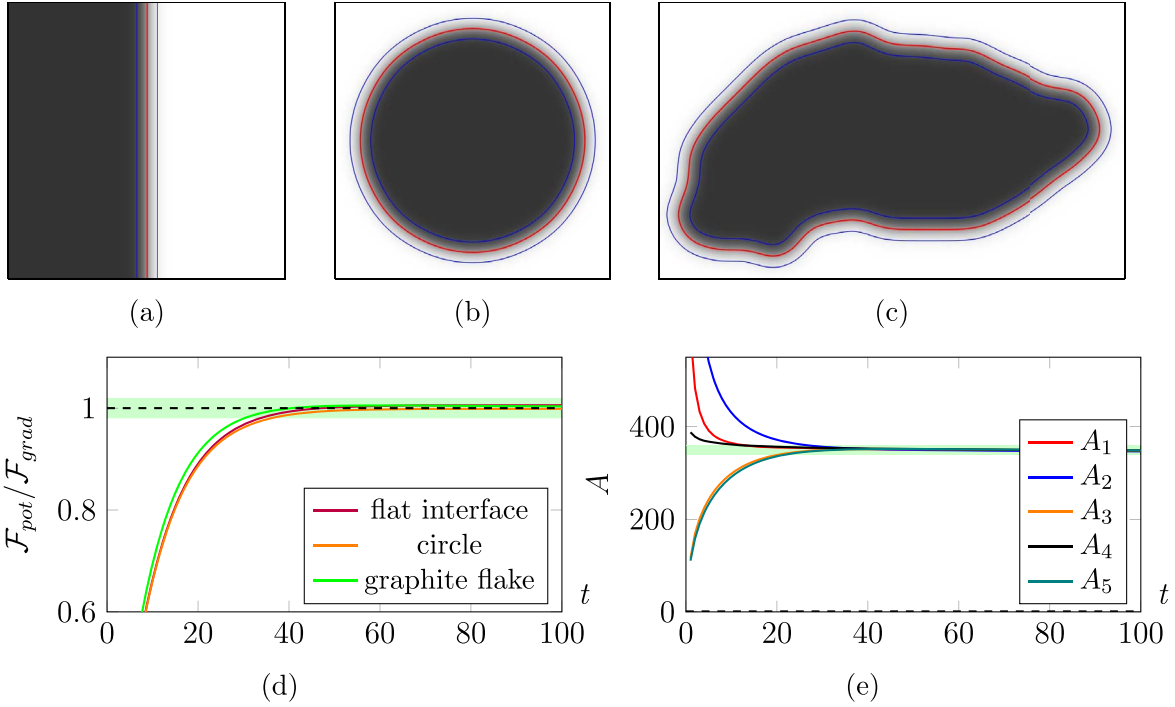
Figure A2. Diffuse representation of (a) flat interface, (b) circle and (c) graphite flake. Red lines represent the line of $\psi = 0.5$ which represents the sharp interface problem. The convergence of interfacial terms is given in subfigure (d) and the corresponding evolution of the length measures for the graphite flake in (e).

$$A_4 = \int_V |\nabla \psi| dV, \qquad [A6]$$

$$A_5 = \int_V \frac{3}{\epsilon} \psi (1 - \psi) dV. \qquad [A7]$$

All surface measures will be compared for various shapes in the following. Note, that the computation of $|\nabla \psi|$ in every cell consumes the most floating point operations and, thus, A_1, A_2 and A_4 take longer to compute while A_5 is the fastest variant.

The results in Fig. A2 reveal important aspects that are intrinsic to the phase-field method. First of all, the convergence of interfacial terms to $\mathcal{F}_{pot}/\mathcal{F}_{grad} = 1$ does not depend on the shape but scales strongly with the interfacial width, i.e. in this case with $\propto \epsilon^2$. The length measures A_2, A_3 and A_5 converge at the same rate as the interfacial ratio because they all have been derived based on the assumption of an equilibrium interface. Length measure A_4 converges much faster which stems from the fact that this is the definition of the surface in a diffuse representation.
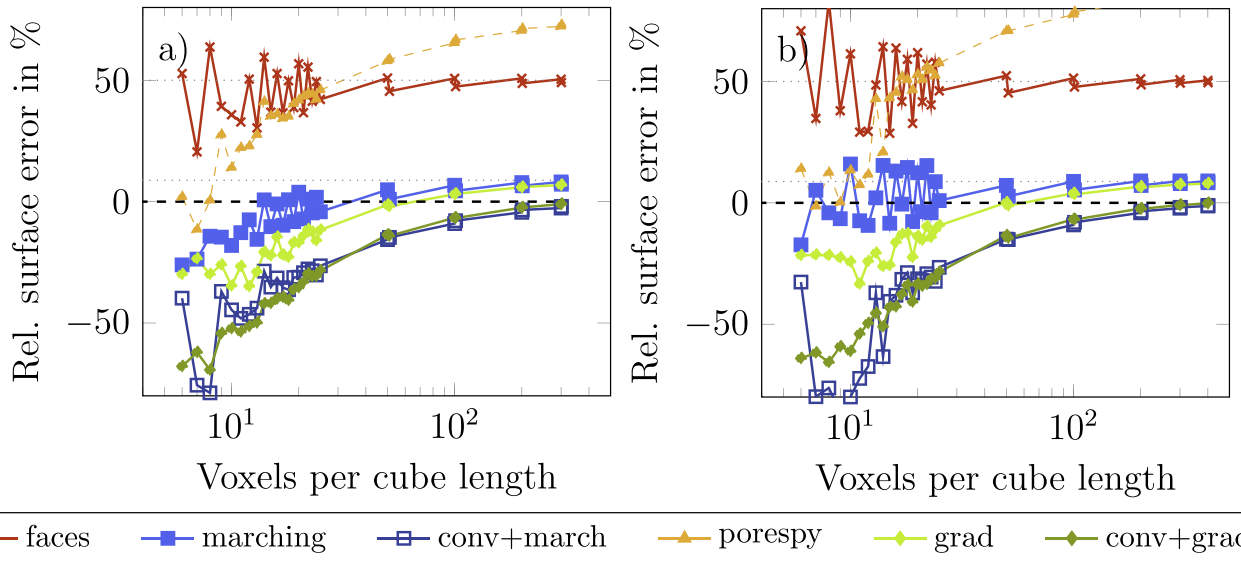
Appendix B. Extended FCC Benchmark Results

Figure B1. Surface area computation on voxelized FCC structure. The relative error of surface area computation is shown for various methods and overlaps of (a) 1% and (b) 5%. The same trends are observed as in Fig. 5b.

ORCID

S. Daubner ⓘ https://orcid.org/0000-0002-7944-6026

References

1. H.-J. Noh, S. Youn, C. Seung Yoon, and Y.-K. Sun, "Comparison of the structural and electrochemical properties of layered Li[Ni$_x$Co$_y$Mn$_z$]O$_2$ (x = 1/3, 0.5, 0.6, 0.7, 0.8 and 0.85) cathode material for lithiumion batteries." *Journal of Power Sources*, **233**, 121 (2013).
2. R. Ruess, S. Schweidler, H. Hemmelmann, G. Conforto, A. Bielefeld, D. A. Weber, J. Sann, M. T. Elm, and J. Janek, "Influence of NCM particle cracking on kinetics of lithium-ion batteries with liquid or solid electrolyte." *J. Electrochem. Soc.*, **167**, 100532 (2020).
3. S. Daubner, M. Weichel, P. W. Hoffrogge, D. Schneider, and B. Nestler, "Modeling anisotropic transport in polycrystalline battery materials." *Batteries*, **9**, 310 (2023).
4. U.-H. Kim, G.-T. Park, B.-K. Son, G. W. Nam, J. Liu, L.-Y. Kuo, P. Kaghazchi, C. S. Yoon, and Y.-K. Sun, "Heuristic solution for achieving long-term cycle stability for Ni-rich layered cathodes at full depth of discharge." *Nature Energy*, **5**, 860 (2020).
5. M. Neumann, T. Philipp, M. Häringer, G. Neusser, J. Binder, and C. Kranz, *Stochastic 3D Modeling of Nanostructured NVP/C Active Material Particles for Sodium-Ion Batteries* (Batteries & Supercaps) 202300409 (2024).
6. T. F. Fuller, M. Doyle, and J. Newman, "Simulation and optimization of the dual lithium ion insertion cell." *J. Electrochem. Soc.*, **141**, 1 (1994).
7. M. Ender, J. Joos, T. Carraro, and E. Ivers-Tiffée, "Quantitative Characterization of LiFePO 4 Cathodes Reconstructed by FIB/SEM Tomography." *Journal of The Electrochemical Society*, **159**, A972 (2012).
8. S. J. Cooper, A. Bertei, P. R. Shearing, J. A. Kilner, and N. P. Brandon, "TauFactor: An open-source application for calculating tortuosity factors from tomographic data." *SoftwareX*, **5**, 203 (2016).
9. W. Schmickler and E. Santos, *Interfacial Electrochemistry, 2nd edn* (Springer Berlin Heidelberg) (2010).
10. D. Fraggedakis, M. McEldrew, R. B. Smith, Y. Krishnan, Y. Zhang, P. Bai, W. C. Chueh, Y. Shao-Horn, and M. Z. Bazant, "Theory of coupled ion-electron transfer kinetics." *Electrochimica Acta*, **367**, 137432 (2021).
11. J. Joos, T. Carraro, A. Weber, and E. Ivers-Tiffée, "Reconstruction of porous electrodes by FIB/SEM for detailed microstructure modeling." *Journal of Power Sources*, **196**, 7302 (2011).
12. F. L. E. Usseglio-Viretta et al., "Resolving the discrepancy in tortuosity factor estimation for Li-ion battery electrodes through micro-macro modeling and experiment." *J. Electrochem. Soc.*, **165**, A3403 (2018).
13. S. Kench and S. J. Cooper, "Generating three-dimensional structures from a two-dimensional slice with generative adversarial network-based dimensionality expansion." *Nature Machine Intelligence*, **3**, 299 (2021).
14. P. Seibert, A. Raßloff, K. Kalina, M. Ambati, and M. Kästner, "Microstructure characterization and reconstruction in Python: MCRpy." *Integrating Materials and Manufacturing Innovation*, **11**, 450 (2022).
15. D. P. Finegan, I. Squires, A. Dahari, S. Kench, K. L. Jungjohann, and S. J. Cooper, "Machine-learning-driven advanced characterization of battery electrodes." *ACS Energy Letters*, **7**, 4368 (2022).
16. microlib: collection of 87 microstructures of various materials, intended for use in materials research. The library is based on the DoITPoMS micrograph library, and made by the tldr group in the Dyson school of Design engineering at Imperial College London. https://microlib.io. Accessed: 2024-06-13 (2024).
17. Github repository with code used for this publication:. https://github.com/daubners/micro-characterization.
18. P. Pietsch, M. Ebner, F. Marone, M. Stampanoni, and V. Wood, "Determining the uncertainty in microstructural parameters extracted from tomographic data." *Sustainable Energy & Fuels*, **2**, 598 (2018).
19. M. C. Krygier, T. LaBonte, C. Martinez, C. Norris, K. Sharma, L. N. Collins, P. P. Mukherjee, and S. A. Roberts, "Quantifying the unknown impact of segmentation uncertainty on image-based simulations." *Nature Communications*, **12**, 5414 (2021).
20. C. Norris, A. Ayyaswamy, B. S. Vishnugopi, C. Martinez, S. A. Roberts, and P. P. Mukherjee, "Uncertainty quantification and propagation in lithium-ion battery electrodes using bayesian convolutional neural networks." *Energy Storage Materials*, **67**, 103251 (2024).
21. V. Laue, O. Schmidt, H. Dreger, X. Xie, F. Röder, R. Schenkendorf, A. Kwade, and U. Krewer, "Model-Based Uncertainty Quantification for the Product Properties of Lithium-Ion Batteries." *Energy Technology*, **8**, 1 (2020).
22. X. Lu et al., "Microstructural evolution of battery electrodes during calendering." *Joule*, **4**, 2746 (2020).
23. S. Kench, I. Squires, A. Dahari, F. Brosa Planella, S. A. Roberts, and S. J. Cooper, "Li-ion battery design through microstructural optimization using generative AI." *Matter*, 1 (2024).
24. W. E. Lorensen and H. E. Cline, "Marching cubes: a high resolution 3D surface construction algorithm." *ACM SIGGRAPH Computer Graphics*, **21**, 163 (1987).
25. scikit-image: Marching cubes. https://scikit-image.org/docs/stable/auto_examples/edges/plot_marching_cubes.html. Accessed: 2024-06-13 (2024).
26. T. Lewiner, H. Lopes, A. W. Vieira, and G. Tavares, "Efficient implementation of marching cubes' cases with topological guarantees." *Journal of Graphics Tools*, **8**, 1 (2003).
27. J. Gostick, Z. Khan, T. Tranter, M. Kok, M. Agnaou, M. Sadeghi, and R. Jervis, "PoreSpy: a python toolkit for quantitative analysis of porous media images." *Journal of Open Source Software*, **4**, 1296 (2019).
28. PoreSpy: Quantitative Image Analysis of Porous Materials. https://porespy.org/examples/metrics/reference/region_surface_areas.html. Accessed: 2024-06-13.
29. J. W. Cahn and J. E. Hilliard, "Free energy of a nonuniform system. i. interfacial free energy." *The Journal of Chemical Physics*, **28**, 258 (1958).
30. R. Kobayashi, "Modeling and numerical simulations of dendritic crystal growth." *Physica D: Nonlinear Phenomena*, **63**, 410 (1993).
31. S. Kench, I. Squires, and S. Cooper, "TauFactor 2: A GPU accelerated python tool for microstructural analysis." *Journal of Open Source Software*, **8**, 5358 (2023).
32. Battery Microstructure Li-Ion Cathode and Anode Data Samples, NMC sample 1-CAL. https://www.nrel.gov/transportation/assets/downloads/caebat/nmc-1-cal-withcbd-w099-binarized.tif. Accessed: 2024-06-13 (2024).
33. J. T. Gostick, "Versatile and efficient pore network extraction method using marker-based watershed segmentation." *Physical Review E*, **96**, 023307 (2017).
34. D. Wang, N. Chen, M. Li, C. Wang, H. Ehrenberg, X. Bie, Y. Wei, G. Chen, and F. Du, "Na 3 V 2 (PO 4) 3 /C composite as the intercalation-type anode material for sodium-ion batteries with superior rate capability and long-cycle life." *Journal of Materials Chemistry A*, **3**, 8636 (2015).
35. P. W. Hoffrogge, D. Schneider, F. Wankmüller, M. Meffert, D. Gerthsen, A. Weber, B. Nestler, and M. Wieler, "Performance estimation by multiphase-field simulations and transmission-line modeling of nickel coarsening in FIB-SEM reconstructed Ni-YSZ SOFC anodes I: Influence of wetting angle." *Journal of Power Sources*, **570**, 233031 (2023).
36. A. Dahari, S. Kench, I. Squires, and S. J. Cooper, "Fusion of Complementary 2D and 3D Mesostructural Datasets Using Generative Adversarial Networks." *Advanced Energy Materials*, **13** (2023).
37. N. Moelans, B. Blanpain, and P. Wollants, "An introduction to phase-field modeling of microstructure evolution." *Calphad: Computer Coupling of Phase Diagrams and Thermochemistry*, **32**, 268 (2008).
38. I. Steinbach, "Phase-field models in materials science." *Modelling and Simulation in Materials Science and Engineering*, **17**, 073001 (2009).
39. S. Daubner, P. W. Hoffrogge, M. Minar, and B. Nestler, "Triple junction benchmark for multiphase-field and multi-order parameter models." *Computational Materials Science*, **219**, 111995 (2023).